*Chem. Mater.* **2006,** *18,* 5130−5136

# Internal Barrier Layer Capacitance Effect in Hexagonal Perovskite $Ba_4YMn_3O_{11.5}$ Ceramics

Xiaojun Kuang, Craig Bridges, Mathieu Allix, John B. Claridge, Helen Hughes, and
Matthew J. Rosseinsky*

*Department of Chemistry, The University of Liverpool, Liverpool, L69 7ZD United Kingdom*

*Received June 1, 2006. Revised Manuscript Received July 10, 2006*

$Ba_4YMn_3O_{11.5}$, a 12R hexagonal perovskite that consists of face-sharing $Mn_3O_{12}$ trimers isolated by single $YO_6$ octahedral layers, is presented. The presence of locally 5- and 6-coordinated $Y^{3+}$ and $Mn^{4+}$ cations is observed in this structure. A high dielectric permittivity ($\epsilon_r \approx 1 \times 10^4$), which is almost frequency independent over the $\sim 1 \times 10^2$ to $1 \times 10^5$Hz range from room temperature to 120 °C, has been observed in ceramics of this material. AC impedance spectroscopy indicates that the internal barrier layer capacitance effect arising from the differing electrical properties of the grains and grain boundaries is responsible for the high dielectric permittivity of this non-ferroelectric material.

## Introduction

The development of faster and smaller microelectronics based on capacitive components requires high-dielectric-permittivity ($\epsilon_r$) materials. Complex perovskites are attracting extensive attention because a dielectric permittivity above $1 \times 10^3$ can be achieved in some materials. There are two classes of high $\epsilon_r$ materials.[1] First, there are the intrinsic ferroelectrics such as $BaTiO_3$-[1] and $PbTiO_3$-based[2] materials, in which ionic spontaneous polarization is the origin of the high dielectric permittivities. A second mechanism is related to extrinsic effects[1] and is caused by polarization of the grain boundary and the electrode−sample interface. Recently, considerable interest has been focused on the cubic perovskite $CaCu_3Ti_4O_{12}$ (CCTO)[3−8] because of its high dielectric permittivity; $\epsilon_r$ values of up to $\sim 1 \times 10^5$ are observed for single-crystal and ceramic samples over a frequency range of $\sim 1 \times 10^2$ to $1 \times 10^6$ Hz and a temperature range of ∼100−400 K, but below 100 K, $\epsilon_r$ drops to ∼100 without an accompanying phase transition. No intrinsic ferroelectric features have been observed for CCTO. It has been suggested, therefore, that the high dielectric permittivity is an extrinsic property of CCTO. Subramanian et al.[3] suggested that twin boundaries in the single crystal can create the observed barrier layer capacitance and account for the dielectric properties, and recently, internal resistive barriers have been found in the crystal from impedance measurements.[8] However, on the basis of impedance spectroscopy measurement of CCTO ceramics, Sinclair et al.[6,7] suggested that the ceramics contain semiconducting grains and insulating grain-boundary regions and that the internal barrier layer capacitance (IBLC) effect from the grain boundaries is responsible for the high dielectric permittivity, thus providing a potential application as an internal barrier layer capacitor. Furthermore, detailed investigation on the development of boundary barrier layers in CCTO ceramics by Fang et al.[9,10] demonstrated that both grain and domain boundary layers are responsible for dielectric response of CCTO. Generally, the crystals of CCTO exhibit larger $\epsilon_r$ values than ceramics, which may suggest that the grain boundaries are not essential for the high permittivity. The nature of the grain boundary and twin boundary effects in CCTO remains controversial.

To the best of our knowledge, most materials exhibiting the IBLC effect with weakly frequency- and temperature-dependent high $\epsilon_r$ are cubic perovskite ceramics, including non-ferroelectric CCTO,[3−7] $AFe_{1/3}B_{2/3}O_3$ (A = Ba, Sr, Ca; B = Nb, Ta, Sb),[11] $La_{0.67}Li_{0.25}Ti_{0.75}Al_{0.25}O_3$ (a lithium conductor),[12] and ferroelectric $BaTiO_3$-based materials such as Ta-doped $BaTi_{0.85}Zr_{0.15}O_3$,[13] with the exception of a non-perovskite Li- and Ti-doped NiO ceramic,[14] among which only the recently reported $La_{0.67}Li_{0.25}Ti_{0.75}Al_{0.25}O_3$[12] has been clearly shown to display the grain-boundary-dominated IBLC effect from impedance spectroscopy measurements. The sole report of the IBLC effect in manganate-based materials is for cubic perovskite-derived $Ca_{1-x}La_xMnO_3$ ($x \leq 0.03$) thin

---

* To whom correspondence should be addressed. E-mail: m.j.rosseinsky@liv.ac.uk.

(1) West, A. R.; Adams, T. B.; Morrison, F. D.; Sinclair, D. C. *J. Eur. Ceram. Soc.* **2004**, *24*, 1439.
(2) Kim, B.; Cho, S. M.; Kim, T.; Jang, H. M. *Phys. Rev. Lett.* **2001**, *86*, 3404.
(3) Subramanian, M. A.; Li, D.; Duan, N.; Reisner, B. A.; Sleight, A. W. *J. Solid State Chem.* **2000**, *151*, 323.
(4) Ramirez, A. P.; Subramanian, M. A.; Gardel, M.; Blumberg, G.; Li, D.; Vogt, T.; Shapiro, S. M. *Solid State Commun.* **2000**, *115*, 217.
(5) Homes, C. C.; Vogt, T.; Shapiro, S. M.; Wakimoto, S.; Ramirez, A. P. *Science* **2001**, *293*, 673.
(6) Sinclair, D. C.; Adams, T. B.; Morrison, F. D.; West, A. R. *Appl. Phys. Lett.* **2002**, *80*, 2153.
(7) Adams, T. B.; Sinclair, D. C.; West, A. R. *Adv. Mater.* **2002**, *14*, 1321.
(8) Li, J.; Sleight, A. W.; Subramanian, M. A. *Solid State Commun.* **2005**, *135*, 260.
(9) Fang, T.; Shiau, H. *J. Am. Ceram. Soc.* **2004**, *87*, 2072.
(10) Fang, T.; Liu, C. P. *Chem. Mater.* **2005**, *17*, 5167.
(11) Raevski, I. P.; Prosandeev, S. A.; Bogatin, A. S.; Malitskaya; M. A. Jastrabik, L. *J. Appl. Phys.* **2003**, *93*, 4130.
(12) Garcia-Martin, S.; Morata-Orrantia, A.; Aguirre, M. H.; Alario-Franco, M. A. *Appl. Phys. Lett.* **2005**, *86*, 043110.
(13) Xu, J.; Itoh, M. *Chem. Mater.* **2005**, *17*, 1711.
(14) Wu, J.; Nan, C.; Lin, Y.; Deng, Y. *Phys. Rev. Lett.* **2002**, *89*, 217601.

10.1021/cm0612752 CCC: $33.50

films,[15] which exhibit a giant dielectric permittivity (~1 × $10^6$ in the 1 × $10^3$ to 1 × $10^5$ Hz range) that is attributed to the IBLC effect. In this study, we present a grain-boundary-dominated IBLC effect in the 12R hexagonal perovskite $Ba_4YMn_3O_{11.5}$, which consists of face-sharing $Mn_3O_{12}$ trimers isolated by single $YO_6$ octahedral layers and, rather unusually, features locally 5- and 6-coordinated $Y^{3+}$ and $Mn^{4+}$ cations. This IBLC effect present a weakly temperature- and frequency-dependent dielectric permittivity of ~1 × $10^4$ over the ~1 × $10^2$ to 1 × $10^5$ Hz range from room temperature to 120 °C for $Ba_4YMn_3O_{11.5}$ ceramics.

## Experimental Section

Polycrystalline powders of $Ba_4YMn_3O_{11.5}$ were prepared via high-temperature solid-state reaction. Stoichiometric amounts of the starting materials $BaCO_3$ (99.997%, Alfa Aesar), $Y_2O_3$ (99.99%, Alfa Aesar), and $MnO_2$ (99.999%, Alfa Aesar) were mixed with acetone in an agate mortar and pestle and calcined in an alumina crucible at 1200 °C for 12 h. This calcined powder was pressed into pellets and fired on platinum foil at 1400 °C for 48 h with several intermediate pressing and grinding steps. The resulting powder was then mixed with a PVA solution binder and pressed into two pellets with diameters of 10 mm and thicknesses of ~5 mm, which were then fired on platinum foil at 1450 °C for 24 h with a 5 °C/min heating rate and cooling rate in air and in oxygen flow, respectively. This resulted in pellets with ~77% relative density. An average oxidation state of 4.01(4) for Mn was determined by an oxalate titration method,[16] which supports the expected formula.

The phase purity of the powder and pellets was checked by X-ray diffraction (XRD) data from both a Panalytical X'pert Pro Multi-Purpose X-ray diffractometer (Co K$\alpha_1$ radiation $\lambda = 1.78901$ Å) and a STOE STADIP X-ray diffractometer (Cu K$\alpha_1$ radiation $\lambda = 1.54051$ Å). Data were collected over a $2\theta$ range of 10−120° for Rietveld refinement on the Stoe diffractometer. Time-of-flight neutron diffraction (ND) data were collected at room temperature on the POLARIS diffractometer at the ISIS facility, Rutherford Appleton Laboratories. Zero-field-cooled (ZFC) and field-cooled (FC) magnetization data were collected using a Quantum Design MPMS SQUID magnetometer from 2−10 K at a field of 200Oe, and ZFC data from 5−400 K at a field of 1000 Oe. Corrections have been applied for the core diamagnetic susceptibility (3.08 × $10^{-4}$ emu/mol).[17] X-ray absorption spectroscopy (XAS) was carried out on station 7.1 at the SRS with $LaMnO_3$ and $CaMnO_3$ as $Mn^{3+}$ and $Mn^{4+}$ standards, respectively. Data were recorded on samples in transmission mode at room temperature across the Mn K edge in ~0.3 eV steps; the Mn metal K edge was run simultaneously as an energy calibration.

AC impedance measurements were carried out from 120 °C to room temperature (RT) using a Solatron 1255B frequency response analyzer and a Solatron 1296 dielectric interface over the frequency range 1 to 1 × $10^6$ Hz. Electrodes were fixed on opposite faces of each pellet by applying a coating of platinum paste, followed by heating at 800 °C for 30 min to burn off the organic components. The impedance data analysis and equivalent circuit fitting were carried out with Zview 2.8 software.[18] The microstructure of the $Ba_4YMn_3O_{11.5}$ ceramic samples was examined using a Hitachi S4800 scanning electron microscopy, and energy dispersive spectroscopy (EDS) analysis was used to examine the compositions.

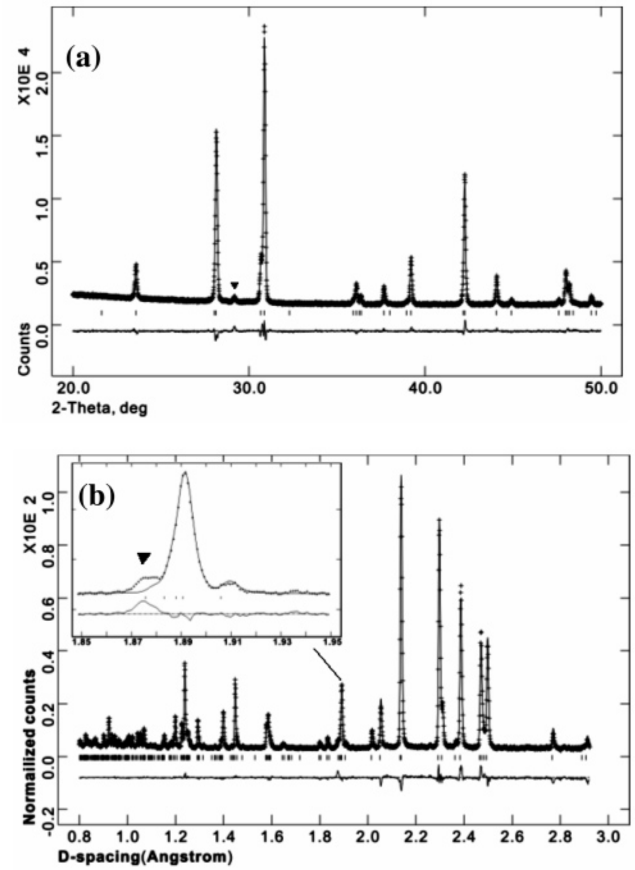

**Figure 1.** Rietveld refinement of (a) XRD data and (b) ND data for $Ba_4YMn_3O_{11.5}$. Peaks from a minor unknown impurity are marked by ▼ in both the XRD an ND patterns.

## Results

The XRD pattern revealed a rhombohedral cell ($a = 5.79$ Å, $c = 28.63$ Å) for $Ba_4YMn_3O_{11.5}$ powder after calcination at 1200 °C for 12 h and 1400 °C for 48 h, similar to that of $Ba_4REMn_3O_{12}$ (RE = $Ce^{4+}$, $Pr^{4+}$).[19] $Ba_4YMn_3O_{11.5}$ thus adopts a 12R-type hexagonal perovskite structure involving a $BaO_3$ stacking sequence of $(cchh)_3$ along the $c$-axis, with face-sharing $Mn_3O_{12}$ trimers connected through corner sharing with $YO_6$ units. The 12R-phase requires synthesis at temperatures above 1300 °C. Rietveld refinement of XRD data (Figure 1a) and ND data (Figure 1b) confirms this structural model with space group $R\bar{3}m$ for $Ba_4YMn_3O_{11.5}$. The oxygen content was refined using the ND data; and the atomic displacement parameters ($U_{iso}$) for all oxygen atoms were constrained to be equivalent in the refinement. The refined oxygen content, $Ba_4YMn_3O_{11.59(7)}$, is in good agreement with the value expected for $Mn^{4+}$ and the outcome of the titrations. The oxidation state of Mn is also confirmed by the XAS data (Figure S1 of the Supporting Information), which shows the same absorption edge energies (6550.9 eV) for both $Ba_4YMn_3O_{11.5}$ and $CaMnO_3$ (6546.8 eV is observed

---

(15) Cohn, J. L.; Peterca, M.; Neumeier, J. J. *J. Appl. Phys.* **2005**, *97*, 034102.

(16) Yang, J.; Song, W. H.; Ma, Y. Q.; Zhang, R. L.; Sun, Y. P. *J. Magn. Magn. Mater.* **2005**, *285*, 417.

(17) Boudreaux, E. A.; Mulay, L. N. *Theory and Applications of Molecular Paramagnetism*; Wiley: New York, 1976.

(18) *Zview for Windows, Impedance/Gain Phase Graphing and Analysis Software*; Scribner Associates, Inc.: Southern Pines, NC.

(19) Fuentes, A. F.; Boulahya, K.; Amador, U. *J. Solid State Chem.* **2004**, *177*, 714.

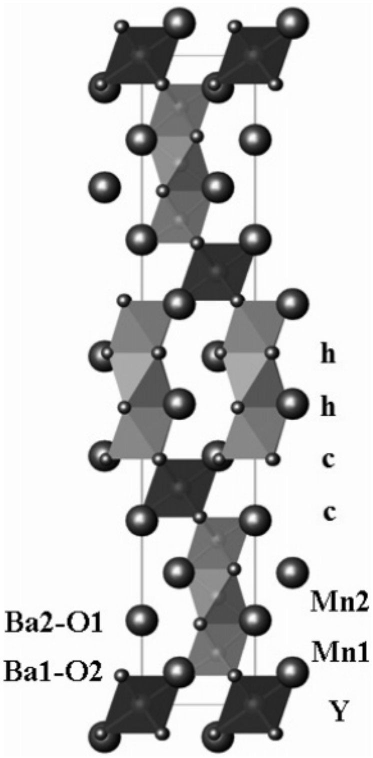

**Figure 2.** Projection along [1 $\bar{2}$ 0] of the crystal structure of $Ba_4YMn_3O_{11.5}$. The $Mn_3O_{12}$ trimers and $YO_6$ octahedra are presented as gray and black, respectively. The larger and small spheres represent Ba and O atoms, respectively.

for $LaMnO_3$). The crystal structure of $Ba_4YMn_3O_{11.5}$ is shown in Figure 2, in which the stacking sequence of $BaO_3$ close-packed layers can be described as $(cchh)_3$ and $Mn_3O_{12}$ trimers are isolated by a single $YO_6$ layer that is linked to the trimers by corner-sharing. Refinement of the site occupancies clearly indicated that all the Y atoms were confined to the corner-sharing sites. The refined structural parameters and bond distances from the ND data are listed in Tables 1 and 2, respectively. An unknown minor impurity was detected in $Ba_4YMn_3O_{11.5}$ (Figure 2a). XRD patterns suggest similar levels of phase purity for pellets of $Ba_4YMn_3O_{11.5}$. The level of impurity is too small to attempt structure solution or to affect the conclusions of this study. Magnetic susceptibility data (Figure 3) reveal a divergence near 4 K between the ZFC and FC data, along with a maximum in the ZFC data at this temperature. In the high-temperature paramagnetic regime, 250−400 K, the effective moment per Mn as deduced by a fit to the Curie−Weiss law is 4.17(1) $\mu_B$; a large, negative Weiss temperature of −447(3) K is obtained.

Figure 4 shows the room-temperature frequency dependence of the dielectric permittivity $\epsilon_r$ and the dielectric loss tan $\delta$ for $Ba_4YMn_3O_{11.5}$ pellets fired at 1450 °C in both air and flowing oxygen. Over the $\sim 1 \times 10^2$ to $1 \times 10^5$Hz frequency range, $\epsilon_r$ shows a plateau at $\sim 1 \times 10^4$ but drops down to $\sim 1 \times 10^2$ to $1 \times 10^3$ in the higher frequency range. The pellet fired in air has a larger $\epsilon_r$ ($\sim$13 000 at $1 \times 10^3$ Hz) than the one fired in flowing oxygen ($\sim$9500 at $1 \times 10^3$ Hz). The tan $\delta$ values at RT for these two pellets are quite similar: the loss is frequency-dependent and reaches a minimum of $\sim$0.9 at 30 kHz. The frequency range of the plateau becomes broader with increasing temperature; a typical plot for the pellet fired in air is shown in Figure 5. Over the measured temperature range, the complex impedance plots $Z''-Z'$ show only one semicircular arc with nonzero intercept at high frequency. Figure 6 shows the $Z''-Z'$ plot at RT for $Ba_4YMn_3O_{11.5}$ pellets. At RT, the arcs have a resistivity ($R$) of $\sim$15 000 Ω cm and associated capacitance ($C$) of $\sim$1 nF cm$^{-1}$ for the pellet fired in air and an $R$ value of $\sim$19 000 Ω cm and a $C$ of $\sim$0.8 nF cm$^{-1}$ for the pellet fired in the oxygen flow. The associated $C$ was estimated from $2\pi f_{max}RC = 1$, where $f_{max}$ is the frequency in hertz at the arc maximum. These processes can be assigned to the grain-boundary response,[21] and the nonzero intercept can be assigned as the bulk resistivity, which indicates that the bulk response is out of the measured frequency range and grain-boundary contributions dominate the dielectric response over the measured frequency range. Each face of a $Ba_4YMn_3O_{11.5}$ pellet was polished by sand paper to reduce the thickness from $\sim$5.2 to 4.7 mm and then to 2.5 mm; the measured RT impedance responses at different stages show no significant change, which confirms that grain boundaries instead of surface layers[22] in the pellets dominate the impedance responses. This in turn indicates that the IBLC microstructure is responsible for the high dielectric permittivity. The impedance response over the measured temperature range can be modeled with an equivalent circuit consisting of a bulk resistance ($R_b$) in series with a parallel set of components $R_{gb}$, $C_{gb}$, and $(CPE)_{gb}$ (a constant-phase element[18]) representing the role of the grain boundary (Figure 6). The $C_{gb}$ values from equivalent circuit fitting[18] (ECF) vary from 0.2$\sim$1.5 nF cm$^{-1}$, which are consistent with the grain-boundary response.[21] The Arrhenius plot of bulk and grain-boundary conductivities of pellets fired in air and flowing oxygen are shown in Figure 7. The activation energies ($E_a$) are 0.242(6) and 0.416(5) eV for bulk and grain boundary, respectively, for the pellet fired in air. Compared with the pellet fired in air, the pellet fired in flowing oxygen shows the same bulk $E_a$ (0.248(5)eV) and a relatively low grain boundary $E_a$ (0.381(5)eV). The grain-boundary activation energies are comparable with those observed in CCTO (0.47−0.63 eV).[6,9] Figure 8 shows the temperature dependence of the dielectric permittivity at different frequencies. In the $1 \times 10^5$ to $1 \times 10^6$ Hz range, the dielectric permittivity increases significantly with increasing temperature, whereas in the $1 \times 10^2$ to $1 \times 10^4$Hz frequency range, the dielectric permittivity shows only weak temperature dependence.

SEM images of fractured sections revealed a porous microstructure (Figure 9a) for $Ba_4YMn_3O_{11.5}$ pellets, as expected for the comparatively low density. The grain sizes were found to lie within the 1−5 $\mu$m range (Figure 9b). EDS elemental analysis on different regions with an area of $\sim$10 $\mu$m$^2$ confirmed that the composition of the material is essentially homogeneous, with the exception of a small number of regions containing less yttrium, which might explain the existence of the minor impurity identified by XRD.

---

(20) Brown, I. D.; Altermatt, D. *Acta Crystallogr., Sect. B* **1985**, *41*, 244.
(21) Irvine, J. T. S.; Sinclair, D. C.; West, A. R. *Adv. Mater.* **1990**, *2*, 132.
(22) Morrison, F. D.; Sinclair, D. C.; West, A. R. *J. Am. Ceram. Soc.* **2001**, *84*, 531.

**Table 1. Refined Structural Parameters and Bond Valence Sums (BVS) for $Ba_4YMn_3O_{11.5}$ from ND Data[a]**

| atom | multiplicity | x | y | z | occupancy | $U_{iso}$ (Å$^2$) | BVS |
|---|---|---|---|---|---|---|---|
| Ba1 | 6c | 2/3 | 1/3 | 0.04965(7) | 1 | 0.0079(4) | 2.04 |
| Ba2 | 6c | 0 | 0 | 0.13008(7) | 1 | 0.0085(4) | 2.04 |
| Y | 3a | 0 | 0 | 0 | 1 | 0.00679(34) | 3.50 |
| Mn1 | 6c | 1/3 | 2/3 | 0.07923(8) | 1 | 0.0031(4) | 3.82 |
| Mn2 | 3b | 1/3 | 2/3 | 1/6 | 1 | 0.0060(6) | 3.91 |
| O1 | 18h | 0.48155(9) | 0.51845(9) | 0.124611(34) | 1 | 0.00866(12)[b] | 1.98 |
| O2 | 18h | 0.48860(11) | 0.51140(11) | 0.288833(30) | 0.933(4) | 0.00866(12)[b] | 2.02 |

[a] Space group: $R\bar{3}m$, $a = 5.787517(34)$ Å, $c = 28.62135(33)$ Å, $Z = 3$. $R_{wp} = 2.86\%$, $R_p = 4.83\%$, and $\chi^2 = 2.34$ for 25 variables. [b] The $U_{iso}$ values for the two different oxygen sites were constrained to be the same. BVS was calculated by Brown's method[20] and the partial occupation of O2 sites was considered in the BVS calculation.

**Table 2. Selected Bond Lengths for $Ba_4YMn_3O_{11.5}$**

| bond | bond length (Å) | bond | bond length (Å) |
|---|---|---|---|
| Ba1−O1 (×3) | 2.8366(18) | Y−O2 (×6)[a] | 2.1928(10) |
| Ba1−O2 (×3)[a] | 3.1119(18) | Mn1−O1 (×3) | 1.9735(17) |
| Ba1−O2 (×6)[a] | 2.89977(13) | Mn1−O2 (×3)[a] | 1.8468(17) |
| Ba2−O1 (×6) | 2.90389(13) | $\Delta d_{Mn1}$ ($1 \times 10^{-4}$)[b] | 11.0 |
| Ba2−O1 (×3) | 2.9171(17) | Mn2−O1 (×6) | 1.9122(9) |
| Ba2−O2 (×3)[a] | 3.0309(19) | Mn1−Mn2 | 2.5025(22) |

[a] The O2 sites are partially (93.3%) occupied. [b] $\Delta d$ is the distortion parameter completed according to $\Delta d = 1/6\sum_{n=1-6}[(d_n - \langle d\rangle)/\langle d\rangle]^2$, where $d_n$ and $\langle d\rangle$ are individual and average bond lengths, respectively.

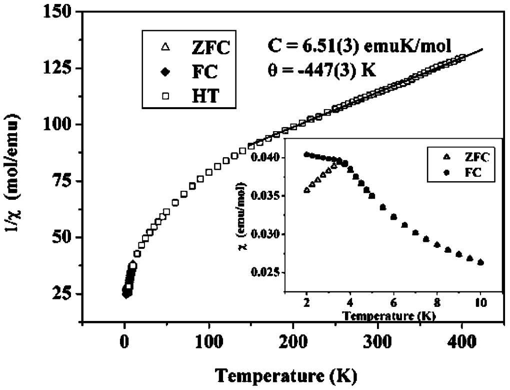

**Figure 3.** Temperature dependence of the inverse magnetic susceptibility of $BaYMn_3O_{11.5}$. The low-temperature ZFC and FC magnetic susceptibilities are shown in the inset. The data labeled HT corresponds to ZFC data in the 5−400 K temperature range. The linear high-temperature region of the inverse magnetic susceptibility data has been fitted to the Curie−Weiss law.

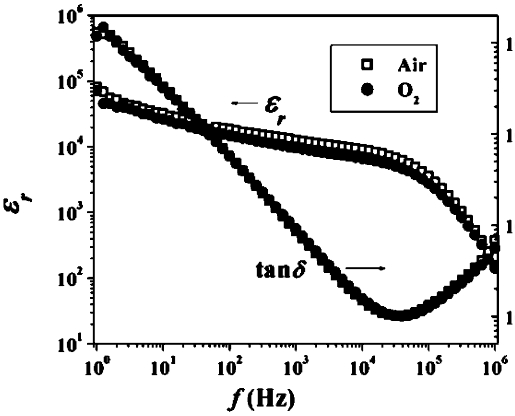

**Figure 4.** Frequency dependence of $\epsilon_r$ and tan $\delta$ values for $Ba_4YMn_3O_{11.5}$ pellets fired in air and flowing oxygen at 1450 °C.

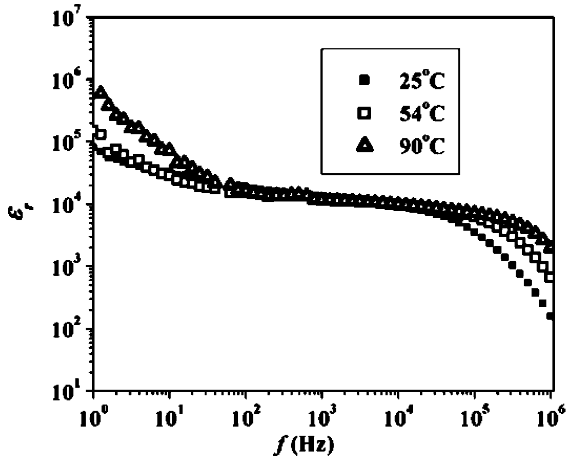

**Figure 5.** Frequency dependence of the relative permittivity $\epsilon_r$ for $Ba_4YMn_3O_{11.5}$ pellets fired in air measured at different temperatures.

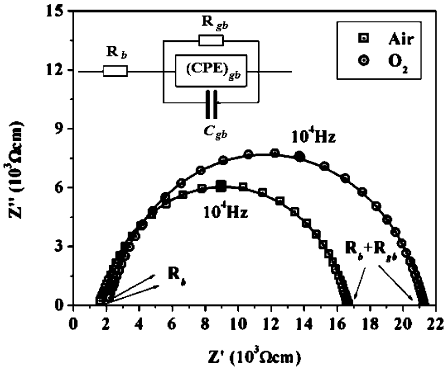

**Figure 6.** Room-temperature (25 °C) complex impedance plot Z″−Z′ for $Ba_4YMn_3O_{11.5}$ pellets fired in air and flowing oxygen at 1450 °C. A selected frequency is shown as filled symbols and the calculated data with the equivalent circuit are shown as a solid line.

## Discussion

The refined oxygen content of 11.59(7) gives a Mn oxidation state of +4 within error, confirmed by the titration and XAS data. Refinement reveals that the O vacancies are located in a disordered manner solely at the O2 sites (Figure 1) within the two c-$BaO_3$ layers rather than the h-$BaO_3$ layers. This results in a coordination number of less than 6 for a significant fraction of the Y and Mn1 species. The mean Mn1 coordination number of 5.80(1) means that 20% of the Mn1 sites at the edges of the trimers are five-coordinate. This is an unusual coordination number for $Mn^{4+}$, although a similar situation has been observed in the analogue $Ba_4InMn_3O_{11.5}$,[23] which shows disordered oxygen vacancies around the In atoms and the outer Mn atoms in the trimers. The mean Y coordination number of 5.60(2) corresponds to 40% of the $Y^{3+}$ cations being five coordinate. This neighboring pyramidal coordination environment for $Mn^{4+}$ and $Y^{3+}$ is quite unusual, especially for the relatively large $Y^{3+}$

---

(23) Créon, N.; Michel, C.; Hervieu, M.; Maignan, A.; Raveau B. *Solid State Sci.* **2003**, *5*, 243.

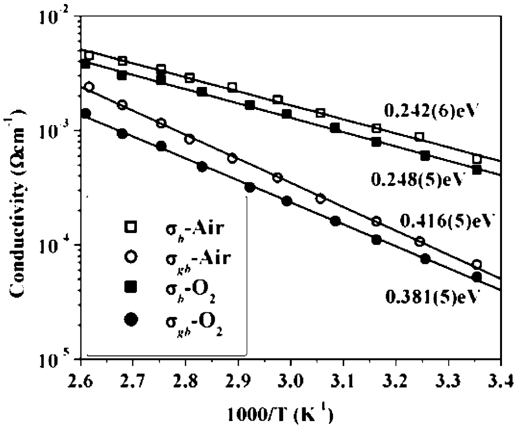

**Figure 7.** Temperature dependencies of bulk and grain-boundary conductivity for $Ba_4YMn_3O_{11.5}$ pellets fired in air and flowing oxygen at 1450 °C.

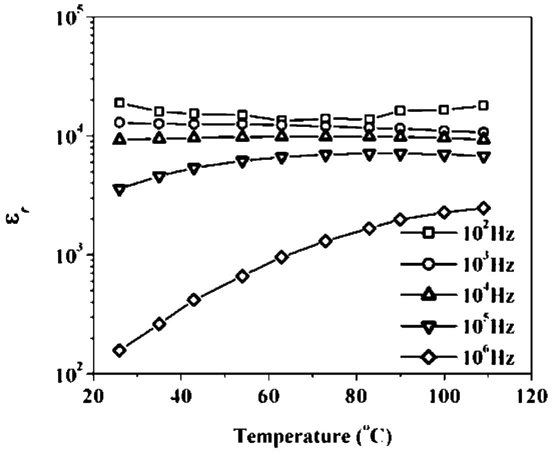

**Figure 8.** The temperature dependence of the relative permittivity $\epsilon_r$ at different frequencies for $Ba_4YMn_3O_{11.5}$ pellets fired in air at 1450 °C.

cations. This material thus represents a rare example of square pyramidal coordination for $Y^{3+}$. The model was carefully examined for the expected structural effects of the presence of oxygen deficiency on the O2 sites. The observed Fourier and difference Fourier maps for $Ba_4YMn_3O_{11.5}$ do not show any significant disordered scattering density around the Y and O2 atom positions. The use of anisotropic atomic displacement parameters does not produce an improvement in the fit, indicating that disordered displacements do not have a significant effect. The BVS for $Mn^{4+}$ within the $Mn_3O_{12}$ trimer are 3.82 for the outer octahedral sites (Mn1) and 3.91 for the central octahedral sites (Mn2); this is in agreement with an oxidation state of 4 for Mn, though the oxygen vacancies around the outer octahedral Mn ions induce weaker bonding to these sites compared with the central Mn2 site. The out-of-center octahedral distortion for the Mn1 sites and the Mn−Mn distance of 2.502(2) Å observed in the $Mn_3O_{12}$ trimer are consistent with those in the analogues $Ba_4REMn_3O_{12}$[19] and $Ba_4InMn_3O_{11.5}$.[23] The BVS of $Y^{3+}$ (3.50 in Table 2) suggests that the $Y^{3+}$ cations are over-bonded, which is consistent with results for other yttrium-containing hexagonal perovskites in which single $YO_6$ layers share corners with face-sharing and/or corner-sharing octahedral blocks such as $Ba_6Y_2Ti_4O_{17}$ (3.49)[24] and $Ba_3YRu_2O_9$ (3.69)[25] and yttrium-containing cubic perovskites such as $A_2YRuO_6$ (A = Ba, Sr) (3.53−3.65).[26−27] This stacking sequence of underbonded Mn1 sites connected by over-bonded Y sites may produce compensating effects, resulting in the overall stabilization of this structure. The calculated values of the global instability index,[28] which measures the degree of structural strain using the bond valence sum of all ions at their formal valences, is 0.13 for this structure, which is within the commonly observed range (less than 0.2) for stable materials. Although the atomic displacement parameters for both oxygen sites were set as the same in order to refine the oxygen content, it was found that if the occupancy of the O2 site was then fixed in the refinement, the refined $U_{iso}$ for O2 was larger than that of O1, which is consistent with partial occupation of the O2 sites. The final point of significance from the structure refinement is that the material clearly adopts a nonpolar space group, ruling out bulk intrinsic explanations of the observed high relative permittivities.

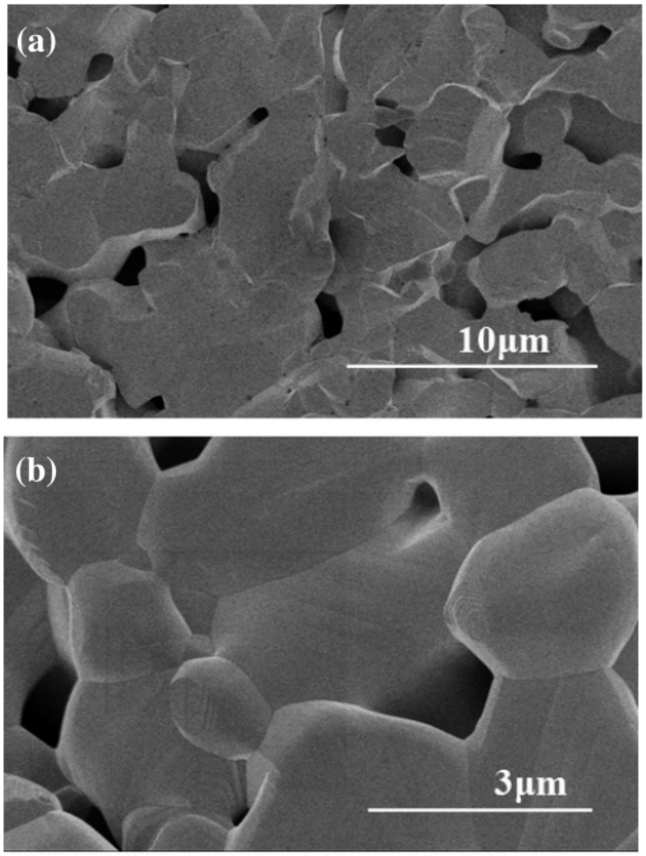

**Figure 9.** SEM images of fractured sections for $Ba_4YMn_3O_{11.5}$ ceramic: (a) porous microstructure and (b) an enlarged area with clear grains and grain boundaries.

The effective moment per Mn, 4.17(1) $\mu_B$, calculated from a fit to the Curie−Weiss law, is slightly higher than the value of 3.89 $\mu_B$ expected on the basis of spin-only magnetism for $Mn^{4+}$ and the value of 3.75 $\mu_B$ observed for the analogue $Ba_4InMn_3O_{11.5}$ in the 150−400 K temperature range.[23] The large, negative value of the Weiss constant (−447(3) K)

---

[24] Kuang, X.; Jing, X.; Loong, C. K.; Lachowski, E. E.; Skakle, J. M. S.; West, A. R. *Chem. Mater.* **2002**, *14*, 4359.

[25] Doi, Y.; Matsuhira, K.; Hinatsu, Y. *J. Solid State Chem.* **2002**, *165*, 317.

[26] Battle, P. D.; Jones, C. W. *J. Solid State Chem.* **1989**, *78*, 108.

[27] Battle, P. D.; Macklin, W. J. *J. Solid State Chem.* **1984**, *52*, 138.

[28] Salinas-Sanchez, A.; Garcia-Munoz, J. L.; Rodriguez-Carvajal, J; Saez-Puche, R; Martinez, J. L. *J. Solid State Chem.* **1992**, *100*, 201.

suggests that strong antiferromagnetic interactions are present within the face-sharing trimers. Because of the strong superexchange interactions that exist between manganese centers connected through face-sharing of octahedra, temperatures above 400 K will be required to access the Curie−Weiss region in $Ba_4YMn_3O_{11.5}$. A high antiferromagnetic ordering temperature is observed in related materials where direct corner-sharing between the face-sharing octahedral units is possible, such as $T_N \approx 278$ K in 4H-$SrMnO_3$.[29] However, for $Ba_4YMn_3O_{11.5}$, the presence of diamagnetic $Y^{3+}$ ions in the octahedra connecting the trimer units by corner sharing imposes a long superexchange pathway between magnetic ions, and hinders the development of long-range correlations, resulting in the absence of clear signatures of magnetic order down to low temperatures.

The FC/ZFC divergence observed at low temperature is suggestive of glassy magnetism, which is evidence for competing exchange interactions and disorder, and is also consistent with the presence of a small quantity of $Mn^{3+}$. This behavior would not be expected in a pure $Mn^{4+}$ perovskite-based lattice, where the dominant exchange interactions would be anticipated to be purely antiferromagnetic. The magnetic data are thus consistent with the presence of a small amount of $Mn^{3+}$. Reduction could occur via oxygen loss during the high-temperature firing in air, resulting in a small O deficiency or inhomogeneity between grains and grain boundaries for $Ba_4YMn_3O_{11.5}$ ceramic samples; this is consistent with the results of the dielectric property measurements detailed below, which reveal a sample dependence related to firing conditions. The magnetic interactions may additionally be frustrated because of the triangular topology of the lattice, and such effects have been proposed to influence the magnetic properties of the related 12R hexagonal perovskite $BaIr_{0.5}Co_{0.5}O_{3.02}$.[30]

The $Ba_4YMn_3O_{11.5}$ ceramics show weakly temperature- and frequency-dependent high dielectric permittivities of about $1 \times 10^4$ over $1 \times 10^2$ to $1 \times 10^5$Hz from RT to 120 °C. This dielectric response is similar to that of CCTO[4] and does not support an explanation based on ferroelectric behavior, i.e., the high dielectric permittivity is not intrinsic but rather arises from the grain-boundary-derived IBLC effect. Room-temperature impedance data (Figure 6) reveal that the $Ba_4YMn_3O_{11.5}$ ceramic comprises insulating grains and even more resistive grain-boundary regions and that the grain-boundary contributions dominate the dielectric response over the measured frequency range. It should be noted that the grains here are more resistive (~2 kΩ cm) than the semiconducting grains found in CCTO[6,7] (~70 Ω cm). This is consistent with the crystal chemistry of the 12R-structured phase compared to the three-dimensional cubic perovskite CCTO: the isolation of the electronically active $Mn_3O_{12}$ trimers by $YO_6$ layers blocks the three-dimensional electronic contact between the $Mn_3O_{12}$ trimers to produce semiconducting grains. In the CCTO case, there is no structural barrier to electronic motion in three dimensions. In contrast, the $Ba_4YMn_3O_{11.5}$ ceramics show more conductive grain boundaries (~15−19 kΩ cm) than those observed in the CCTO[6−7] ($R_{gb} \approx 0.2-4$ MΩ cm). The relative small total resistivity (~20 kΩ cm) observed for $Ba_4YMn_3O_{11.5}$ ceramics gives higher tan $\delta$ values of ~0.9−40 in $1 \times 10^2$ to $1 \times 10^6$Hz (in Figure 4) (compared with tan $\delta \approx 0.04-0.2$ in $1 \times 10^2$ to $1 \times 10^6$Hz for CCTO).[6−7] The difference between the resistivities of grains and grain boundaries is relatively smaller for this material, which differs from the classical CCTO and $BaTiO_3$-type materials. The observed high permittivity and high tan $\delta$ give $Ba_4YMn_3O_{11.5}$ more common features with high-dielectric-permittivity ferrites such as $BaCo_{2-x}Zn_xFe_{16}O_{27}$[31] and Cu-containing ferrites,[32] which has been ascribed to either an inhomogeneous microstructure[33] consisting of well-conducting grains and separate, more resistive grain boundaries (the Maxwell−Wagner model, i.e., the IBLC effect) and/or electric charge (n- and p-type) hopping contribution to dielectric polarization (Rezlescu model).[34] However, the dielectric behavior of the ferrites generally exhibits strongly frequency- and temperature-dependent permittivity and significant relaxation phenomena over the $1 \times 10^2$ to $1 \times 10^5$ Hz frequency range,[31−35] in which the present material differs significantly from the ferrites.

The hypothetical oxygen stoichiometric parent pure $Mn^{4+}$ $t_{2g}^3$ phase $Ba_4YMn_3O_{11.500}$ would be expected to be a Mott−Hubbard insulator by analogy with $CaMnO_3$. The electronic isolation of the d-electron-bearing $Mn_3O_{12}$ trimers by the closed-shell $YO_6$ sites reinforces this tendency. Introduction of $Mn^{3+}$ centers by generation of oxygen vacancies (e.g., by reducing the oxygen partial pressure from pure oxygen to air) would increase the conductivity by the well-established doped Mott insulator mechanism.[36] The presence of small quantities of $Mn^{3+}$ to produce enhanced conductivity is also consistent with the competing superexchange interactions observed in the spin glass behavior at low temperature. This picture suggests that small variations in oxygen content (below the level of sensitivity of the characterization methods we have applied here) at high temperature for $Ba_4YMn_3O_{11.5}$ during processing are responsible for modifying the IBLC behavior. The higher bulk and grain-boundary resistances observed when firing in the oxygen flow as compared with the pellet fired in air suggest that the electronic properties of $Ba_4YMn_3O_{11.5}$ are strongly influenced by small changes in band filling driven by modification of the oxygen content, in line with the above scenario. Assuming that this small concentration of O vacancies and associated $Mn^{3+}$ carriers is generated at high temperature, limited reoxidation along the grain-boundary regions during the cooling procedure could occur to produce higher resistance for the grain-boundary regions than for the grains; the grain boundaries would be expected to have a lower oxygen vacancy content and a reduced concentration of $Mn^{3+}$ carriers, thus forming

---

(29) Battle, P. D.; Gibb, T. C.; Jones, C. W. *J. Solid State Chem.* **1988**, *74*, 60.
(30) Vente, J. F.; Battle, P. D. *J. Solid State Chem.* **2000**, *152*, 361.
(31) Ismael, H.; El Nimr, M. K.; Abou El Ata, A. M.; El Hiti, M. A.; Ahmed, M. A.; Murakhowskii, A. A. *J. Magn. Magn. Mater.* **1995**, *150*, 403.
(32) Zaki, H. M. *Physica B* **2005**, *363*, 232.
(33) Koops, C.G. *Phys. Rev.* **1951**, *83*, 121.
(34) Rezlescu, N.; Rezlescu, E. *Solid State Commun.* **1974**, *14*, 69.
(35) Abou E. L.; Ata, A. M.; El Hiti, M. A. *J. Phys. III* **1997**, *7*, 883.
(36) Mott, N. F. *Metal-Insulator Transitions*; Taylor & Francis: London, 1974.

internal barrier layers to produce a high permittivity. Thermogravimetric analyses (TGA) in an air, oxygen, and nitrogen flow from RT to 1000 °C on $Ba_4YMn_3O_{11.5}$ powder from a pellet fired in air at 1450 °C were used to detect mass variation due to the limited reoxidation along grain-boundary regions. No obvious mass change was observed in the TGA data, which suggests the change of oxygen content involved is too small to be detected. This kind of IBLC effect arising from the different level of oxygen deficiency in different regions within ceramic samples has been well-established for the multistep ferroelectric $BaTiO_3$-type materials.[37] Heterogeneity in the cation stoichiometry also plays an important role in driving the IBLC effect, as indicated by studies of the defect chemistry of CCTO.[38−39] The latest report of the effect of Mn-doping on the semiconducting properties of CCTO ceramics[40] shows that a small amount (∼2 at %) of substitution of Mn onto the Cu site suppresses the semiconductivity of the CCTO ceramic by 6 orders of magnitude; the bulk of Mn-doped CCTO shows conduction behavior similar to that of the grain boundaries of CCTO ceramic, which implies that slight differences in the cation composition from the semiconducting bulk for CCTO is enough to produce insulating grain boundaries to drive the IBLC effect instead of the necessary secondary phase. Therefore, the slight anion and/or cation compositional difference between grains and grain boundaries is an effective method for tuning the extrinsic properties of materials that show IBLC effects.

Comparison of the pellets fired in air and flowing oxygen shows that the higher bulk and grain-boundary conductivities obtained by processing in air give a higher dielectric permittivity. The interpretation of this relationship between conductivity and permittivity may be correlated with the defects associated with oxygen loss (oxygen vacancies, electrons, and $Mn^{3+}$ centers) because the size of the conductivity is closely related with the presence of the defects. The pellet fired in air has a higher concentration of defects in the bulk and grain boundary compared with the pellet fired in flowing oxygen. The almost identical activation energies of bulk conduction for these pellets and the relatively lower activation energies of grain-boundary conduction observed for the pellet fired in flowing oxygen implies that the difference between the defect content in the grain-boundary regions for these two pellets is much more significant than that between the defect content in bulk. This also suggests the firing atmosphere has a greater influence on the grain boundary rather than the bulk.

## Conclusions

An IBLC effect with a dielectric permittivity plateau of $\sim 1 \times 10^4$ over the $\sim 1 \times 10^2$ to $1 \times 10^5$ Hz range from room temperature to 120 °C with a weak temperature dependence was observed in non-ferroelectric $Ba_4YMn_3O_{11.5}$ ceramics. This phase adopts a 12R-type hexagonal perovskite structure in which $Mn_3O_{12}$ trimers are electronically isolated by a single yttrium octahedral layer. $Ba_4YMn_3O_{11.5}$ ceramic samples contain insulating grains and more resistive grain-boundary regions. The isolation of $Mn_3O_{12}$ trimers by yttrium octahedral layers results in insulating behavior of the grains, but this insulating behavior appears tunable via oxygen loss at high temperature and incomplete reoxidation on cooling. Limited reoxidation along grain-boundary regions might be responsible for their higher resistance than that of the grains, and create an IBLC effect to produce a high dielectric permittivity for $Ba_4YMn_3O_{11.5}$. A direct link between the dielectric permittivity and the conductivities of grains and grain-boundary regions was found. Although the tan $\delta$ values are quite high for this material, which would restrict its application as an IBLC capacitor, the observation of high dielectric permittivity in ceramics of the 12R-type hexagonal $Ba_4YMn_3O_{11.5}$, in which the conducting/magnetic units are isolated from each other by strongly insulating barriers (the $Y^{3+}$ cations here), is interesting. This study suggests that this family of complex hexagonal perovskite may allow for compositional tuning of extrinsic ceramic properties and could contribute to the understanding of the class of IBLC materials.

**Acknowledgment.** The authors thank Dr. C. Auener (Department of Chemistry, University of Liverpool) and Dr. R. I. Smith (ISIS Rutherford Appleton Lab) for their help in collecting the neutron diffraction data, Stephen Apter (Department of Chemistry, University of Liverpool) for ICP elemental analysis, and Peter Beahan (Department of Engineering, University of Liverpool) for assistance with SEM experiments. We thank EPSRC for support under EP/C511794/1. M.J.R. thanks the Royal Society for a Wolfson Research Merit Award.

**Supporting Information Available:** Crystallographic information in CIF format and X-ray absorbtion spectroscopy plot in PDF format. This material is available free of charge via the Internet at http://pubs.acs.org.

CM0612752

---

(37) Yang, C. *Jpn. J. Appl. Phys., Part 1* **1996**, *35*, 1806.

(38) Li, J.; Subramanian, M. A.; Rosenfeld, H. D.; Jones, C. Y.; Toby, B. H.; Sleight, A. W. *Chem. Mater* **2004**, *16*, 5223.

(39) Fang, T.; Mei, Li.; Ho, H. *Acta Mater.* **2006**, *54*, 2867.

(40) Li, M.; Feteira, A.; Sinclair, D. C.; West, A. R. *Appl. Phys. Lett.* **2006**, *88*, 232903.